Supplementary information

Fabrication methods

The Si microwire arrays were grown by a photolithographically patterned $SiCl_4$ VLS process, as described previously, using BCl_3 for p-type doping and 300 nm Cu as the catalyst.[1-3] Following growth, the Cu catalyst was removed by etching the wire arrays for 30 s in 5% HF(aq), for 20 min in 6:1:1 by volume H_2O:H_2O_2(30% in H_2O):conc. HCl(aq) at 75 °C, and for 60 s in 20 wt % KOH(aq) at 20 °C. A conformal SiO_2 diffusion-barrier (~200 nm thick) was grown by dry thermal oxidation for 2 hr at 1100 °C. The wire arrays were then partially infilled with poly-dimethylsiloxane (PDMS), as described previously.[6] Briefly, wire array samples were coated with a solution that contained 4.4 g hexamethylcyclotrisiloxane (Sigma-Aldrich), 1 g PDMS (Sylgard 184, Dow Corning), and 0.10 g curing agent in 5 ml of dichloromethane; spun at 1000 RPM for 30 s; and cured for 30 min at 150 °C, producing a 10–15 μm thick PDMS layer at the base of the wire array (thicker infill layers were achieved by repeating this process up to 4 times). The partially infilled arrays were etched for 5 min in buffered HF (BHF) to remove the exposed diffusion-barrier oxide, then the PDMS was removed by etching for 30 min in a solution of 1.0 M tetra-n-butylammonium fluoride made using a 1:1 (vol) mixture of tetrahydrofuran and dimethylformamide.[7] A 10 min piranha etch (3:1 aq. conc. H_2SO_4:30% H_2O_2) was also performed to remove any residual organic contamination.

To form the radial p-n junctions, the wire arrays were etched for 5 s in 10% HF(aq), then thermal P diffusion was performed for 10 min at 850 °C using CeP_5O_{14} source wafers (Saint-Gobain, PH-900), followed by a 30 s deglaze in BHF. Spreading resistance measurements (Solecon Laboratories) on Si control wafers indicated a junction depth of 100 nm and a surface dopant concentration of 1×10^{19} cm^{-3}. Individual microwires were removed from the array using a razor blade, suspended in isoproponal, and dispersed onto sapphire or SiN_x/Ag-coated-Si wafers.* Ag-capped Al contacts were photolithographically patterned as described previously.[4]

The PECVD a-Si:H was deposited at 240 °C and 500 mTorr, using 5% SiH_4 in Ar at a total flow rate of 100 sccm, and a 13.56 MHz plasma at 3 W forward power. A 30 min deposition time was chosen to produce a ~10 nm-thick layer of nominally intrinsic a-Si:H on the wire sidewalls. After metallization, the a-Si:H-coated single-wire devices required a 30 min anneal at 275 °C in forming gas (5% H_2 in N_2) to produce ohmic contacts through the a-Si:H layer. The a-SiN_x:H was deposited at 350 °C and 1 Torr in a parallel-plate reactor (Plasmalab System100, Oxford Instruments), using a SiH_4/NH_3 gas chemistry whose ratio was chosen to produce films that had a refractive index of ~2.0 (400 sccm 5% SiH_4 in N_2, 30 sccm NH_3). In-situ stress control was performed by alternating between a 3.56-MHz and 50-kHz plasma frequency, both with 20 W of forward power (65% RF duty cycle). Deposition was performed for 25 min, producing a coating that varied from ~60 nm thick at the wire base to ~120 nm thick at the wire tip, as observed by cross-sectional SEM (Fig. S3). Prior to removing wires from the growth substrate, the a-SiN_x:H-coated arrays were partially infilled with wax (Quickstick 135, South Bay Tech.) and then etched for 10 s in 49% HF(aq) to remove the a-SiN_x:H from the uppermost ~10 μm of each wire,[8] enabling the formation of single-wire contacts.

I–V measurements were performed with a four-point source-measure unit (Keithley 238). Simulated sunlight was provided by a 1000 W Xe arc lamp with AM 1.5G filters (Oriel) calibrated to 1-sun illumination (100 mW•cm^{-2}) by an NREL-traceable Si reference cell (PV Measurements).

* Sapphire substrates: 2", 350 μm thick, double-side-polished C-plane wafers. Ag substrates: 3" n^+ Si <100> wafers, top-side-polished, coated with 100 nm Ag by thermal evaporation (for reflectivity), then with 200–300 nm SiN_x by PECVD as described above (for insulation).

Characterization of PECVD films

Note: Some of the information and figures regarding the a-SiN$_x$:H films also appear as supplementary information for reference (5). The research for both studies was carried out concurrently using identical a-SiN$_x$:H deposition conditions.

In this study, amorphous hydrogenated films of silicon (a-Si:H) and silicon nitride (a-SiN$_x$:H) were deposited by plasma-enhanced chemical vapor deposition (PECVD) onto Si wire-arrays to serve as anti-reflective and/or surface-passivation layers. The optical properties of both film types were measured by depositing them onto planar Si wafers and performing multiple-angle spectroscopic ellipsometry. Ψ and Δ spectra, ranging from 350–2200 nm, were measured at angles of 60°, 65°, and 70° (as shown in Fig. S1a for an a-SiN$_x$:H film). The spectra were then fit to a Forouhi-Bloomer model for amorphous dielectric materials.[9] The real and imaginary parts of the index produced by the fit are plotted in Figures S1b and S2 for a-SiN$_x$:H and a-Si:H, respectively. These values were used for the optical modeling of Si wire solar cells presented elsewhere in this study.

The thickness profile of the a-SiN$_x$:H films deposited onto the Si wires was measured by SEM, using focused-ion beam (FIB) milling to produce wire cross-sections (Fig. S3). Individual wires were removed from the growth substrate and deposited (horizontally) onto a Si wafer, then blanket-coated by the same Al/Ag metal layers used to form electrical contacts elsewhere in this study (in this the metal served to facilitate milling and imaging). The deposited nitride thickness increased gradually along the length of the wires, reaching ~2× the base thickness at the top sidewall of the wire, and ~2.5× the base thickness on the top surface of the wires. Average sidewall deposition rates were ~4× slower than those produced on planar structures. For this study, the deposition was performed for 25 min to target wire-sidewall nitride-thicknesses ranging from ~60 nm at the wire bases to ~120 nm at the wire tips. The a-Si:H film thickness was not directly imaged on Si wire surfaces. However, the deposition rate was calibrated for planar control structures, using ellipsometry to measure film thicknesses, and the deposition time was extended by 4× to produce the desired film thickness (~10 nm) on the wire sidewalls.

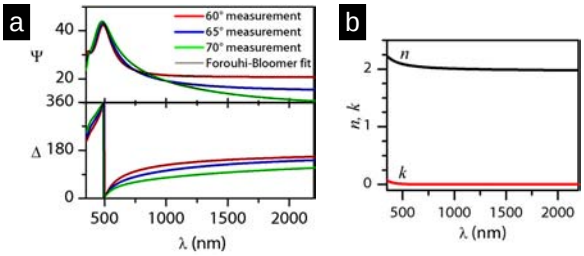

Figure S1. Characterization of PECVD a-SiN$_x$:H by spectroscopic ellipsometry. *These plots also appear as supplementary figure S2 in reference (5).*

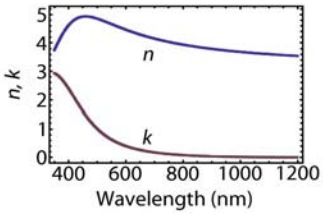

Figure S2. Optical properties of PECVD a-Si:H as determined by spectroscopic ellipsometry.

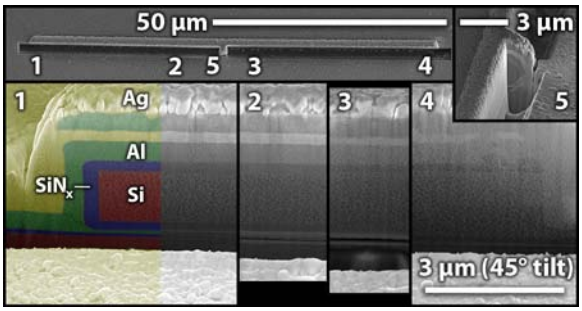

Figure S3. Cross-sectional SEM images of an a-SiN$_x$:H-coated wire, showing nitride thickness variation along the length of the wire, as well as the structure of the evaporated Al/Ag films used for contact electrodes in this study. Partial false-coloring added for clarity. *This image also appears as supplementary figure S1 in reference (5).*

Scanning photocurrent microscopy

Scanning photocurrent microscopy (SPCM) measurements have been widely used to study carrier transport within semiconductor nanowire and microwire structures.[1,4,10-13] In this study, SPCM measurements were performed using a confocal microscope in a light-beam-induced current (LBIC) configuration as described previously.[1,4] A chopped laser source (λ = 650 nm for bulk excitation or λ = 405 nm for surface excitation) was focused to a diffraction-limited spot size through a 50×, N.A. = 0.95 microscope objective, and the induced specimen photocurrent was recorded using lock-in detection. SPCM images were formed by rastering the single-wire devices beneath the beam.

Prior to each measurement, the incident beam intensity was measured with a calibrated photodiode, allowing the specimen current to be reported in terms of the external quantum efficiency (E.Q.E.). A typical beam photocurrent of 20–200 nA was used, which induced peak specimen photocurrent values of the same approximate magnitude as each device's 1-sun I_{SC}. We note, however, that all devices exhibited nominally identical SPCM profiles under ~2000× lower illumination levels (Fig. S4), indicating that the observed recombination rates were not an effect of higher injection levels than would be present within each wire under 1-sun illumination. The SPCM profiles were found to be insensitive to sample bias (ranging from −1 to 0.4 V), and were also not affected by the application of broad-area illumination that was previously shown to temporarily reduce surface recombination in p-type VLS-grown Si microwires with native-oxide-terminated surfaces.[1] Unless noted, all SPCM measurements reported in this study were performed at short-circuit (zero bias voltage) using λ = 650 nm excitation under otherwise dark conditions.

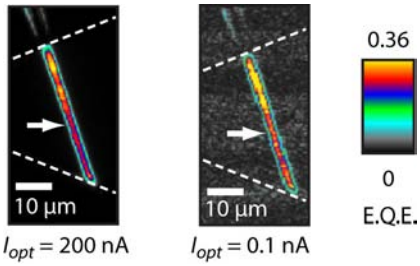

Figure S4. SPCM profiles of an a-SiN_x:H-coated device measured under typical (I_{opt} = 200 nA) and reduced (I_{opt} = 0.1 nA) excitation intensity. The dashed white lines indicate the location of the contacts, and the arrows indicate start of radial p-n junction.

Passivation with hydrofluoric acid

For this study, some SPCM measurements were performed on single-wire devices that were fully immersed in buffered hydrofluoric acid (BHF). Hydrofluoric acid is known to effect unusually low surface recombination velocities at Si surfaces ($S < 1$ cm·s^{-1}).[14] To enable these measurements, single-wire devices were fabricated on sapphire substrates to provide the necessary stability under BHF immersion. (For consistency, all other SPCM devices were also fabricated on sapphire substrates.) The devices were then covered with a positive photoresist layer (S1813, Microchem) to protect the metal contacts from corrosion. The photoresist was patterned and developed to expose a well over the central portion of each wire (Fig. S5a) and to expose the contact bond pads (located several mm away). To extend the longevity of the photoresist under BHF immersion, the devices were baked at 115°C for ~2 min shortly before beginning the measurements. Initial *I–V* behavior and SPCM profiles were recorded to determine the properties and extent of the radial p-n junction within each device (Figs. S5b and S5d). A droplet of pH = 5.0 BHF (Transene) was then placed over the wire and covered by a small plastic coverslip to prevent evaporation and enable imaging through the liquid.

For the first 1–3 min of immersion in BHF (before the SiO_2 diffusion-barrier was etched away), the wires exhibited no noticeable change in SPCM behavior. Once the surface oxide had

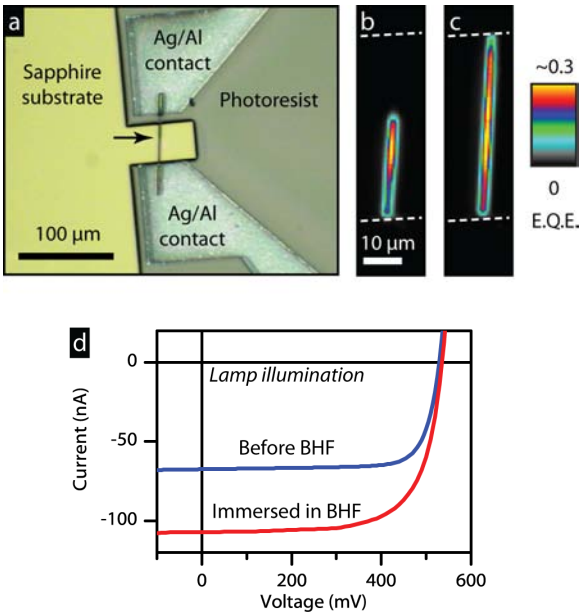

Figure S5. SPCM measurements of single Si wire devices passivated by buffered HF (BHF). **a,** Microscope image of the test structure. **b,c,** SPCM profiles of the exposed wire area before (b) and after (c) immersion in BHF. Dashed lines indicate the location of metal contacts. The reduced spatial resolution of these SPCM profiles was due to the use of a 20x, N.A. = 0.4 objective to provide greater working distance. **d,** Light *I-V* behavior under microscope lamp illumination, measured before and during immersion in BHF.

been removed, collection was observed from throughout the axial region of the wire (Fig. S5c). Because each SPCM image acquisition required ~3 min to complete, we were unable to observe the dynamics of the transition. The SPCM behavior indicated an effective carrier collection length, L_{eff}, of >> 20 µm (the longest axial wire length studied by this technique). Light *I–V* measurements, performed under broad-area illumination from the microscope's halogen lamp, showed an increase in I_{SC} that was roughly commensurate with the increase in active area observed by SPCM (Fig. S5d). The SPCM and *I–V* behavior of the BHF-immersed devices remained essentially constant for another 10–30 min, after which time the contacts began to corrode (starting with the evolution of bubbles beneath the photoresist that quickly grew so as to preclude further SPCM measurements). The devices were then rinsed and dried, after which some exhibited open-circuit behavior (due to the wire or contact structure having been washed away), while others exhibited SPCM profiles similar to that observed prior to BHF immersion (i.e., L_{eff} < 0.5 µm).

Prior to removal from the growth substrate, some wires had also been etched in BHF to fully remove the SiO_2 diffusion-barrier from the axial region. These wires also showed L_{eff} < 0.5 µm behavior under SPCM, confirming that a high axial-region surface recombination velocity also existed at native-oxide-terminated surfaces.

Determination of junction position and minority-carrier collection length

Non-passivated wires: SPCM measurements on non-passivated wires indicated a very short L_{eff} within the axial portion of each wire. In fact, the decay in carrier collection within these regions could not be resolved by the ~0.5 µm-diameter diffraction-limited spot size of the illumination source. Figure S6 shows the log-scale SPCM profile of a typical non-passivated wire device, illustrating how the spatial decay in photocurrent along the axial direction of the wire occurred as abruptly at the end of the radial junction as at it did at the edge of the metal contacts. The abrupt transition from radial to axial carrier collection clearly identified the endpoint of the radial p-n junction within each wire, and always occurred at the edge of the SiO_2 diffusion-barrier oxide (when such was present, e.g., as shown in Figure 3a of the manuscript).

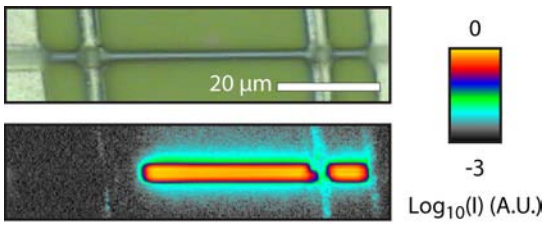

Figure S6. Microscope image (top) and log-scale SPCM image (bottom) of a typical non-passivated single-wire test structure.

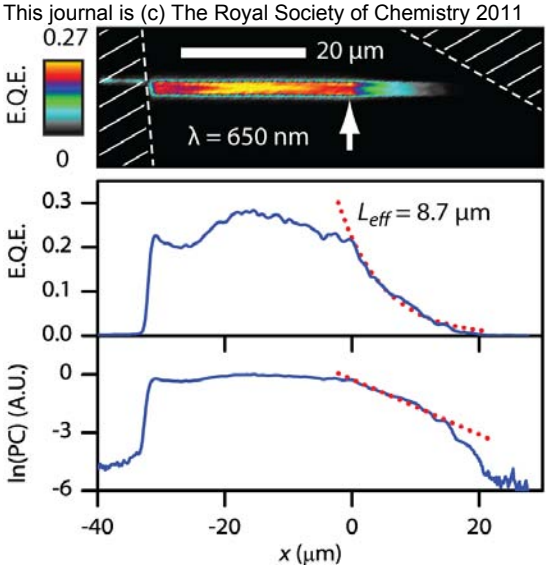

Figure S7. Cross-sectional SPCM profile of an a-Si:H-coated single-wire device. Top: SPCM image, with the metal contacts and the start of the radial p-n junction indicated by the white hashed areas and arrow, respectively. Below: Linear-scale (center) and log-scale (bottom) cross-sections of the above SPCM data, taken along the center of the wire, with dotted line indicating exponential fit to data. Data is aligned so that the axial region started at $x > 0$ μm.

a-Si:H-coated wires: SPCM measurements on a-Si:H-coated wires indicated exponentially-decaying carrier collection along the axial length of each wire, as expected for transport limited by minority-carrier diffusion within the quasi-neutral region of a p-n junction device. Figure S7 plots linear- and log-scale cross-sections of the SPCM profile of the a-Si:H-coated device from Fig. 3c. Approximately constant E.Q.E. was observed throughout the radial portion of the wire ($x < 0$ μm), while exponentially decaying E.Q.E. was observed in the axial portion of the wire ($x > 0$ μm). A fit to the exponential decay indicated L_{eff} = 8.7 μm for this device. Six a-Si:H-coated single-wire devices were studied by SPCM, and L_{eff} values ranging from 5.4–9.8 μm were observed.

Because the SiO_2 diffusion-barrier had been removed from the a-Si:H-coated wires, the spatial extent of the axial region could not be directly observed by optical microscopy. Thus, the endpoint of the radial p-n junction was inferred from the SPCM profiles of each wire,

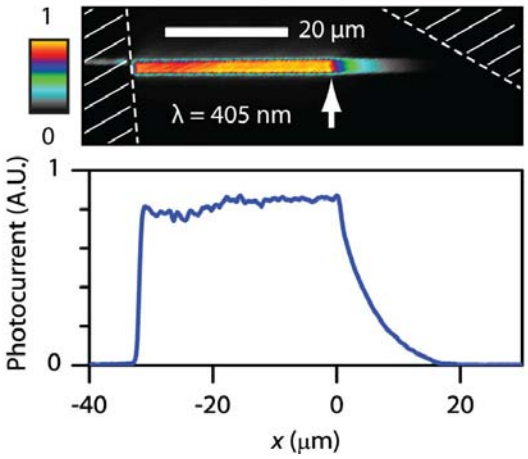

Figure S8. SPCM image (above) and linear-scale cross-section (below) of the wire shown in Fig. S7, acquired using a λ = 405 nm illumination source.

assumed to occur at the onset of exponentially decaying E.Q.E. However, minor fluctuations in E.Q.E. were also observed throughout the entire wire, obfuscating the transition between radial and axial collection. We believe that these fluctuations arose from photonic effects rather than from variations in the carrier-collection-efficiency along the wires. At the illumination wavelength (λ = 650 nm), the optical absorption properties of Si microwires are dominated by scattering and dielectric resonance effects, which depend strongly on the wire diameter.[15] The diameters of our wires varied and generally decreased slightly from base to tip, with a typical taper of 10–20% observed by SEM (see Fig. S3). To demonstrate that the radial-region carrier-collection-efficiency was approximately uniform, we performed SPCM measurements with a λ = 405 nm illumination source, at which wavelength the Si microwires were optically opaque and thus less affected by dielectric resonances. Figure S8 shows the λ = 405 nm SPCM image of the same a-Si:H-coated wire, which exhibits a more-uniform carrier-collection efficiency within the radial region of the wire, as well as a more-pronounced transition to exponentially decaying behavior within the axial region of the wire.

a-SiN_x:H-coated wires: SPCM measurements on a-SiN_x:H-coated wires indicated relatively constant E.Q.E. throughout the entire non-

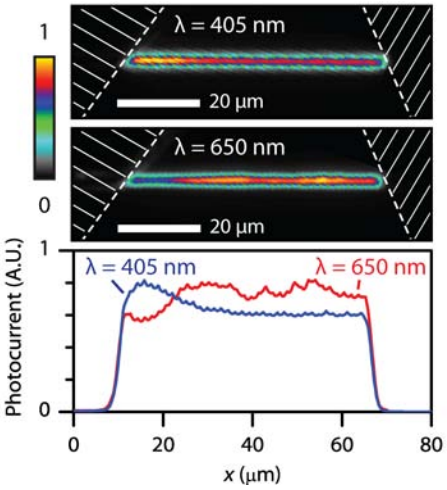

Figure S9. SPCM measurements of an a-SiN_x:H-coated single-wire device, measured with λ = 405 nm (upper) and λ = 650 nm (lower) illumination sources. Below: normalized cross-sections of the above profiles. The radial p-n junction extends from beneath the left contact.

shaded extent of each wire, indicative of large values of L_{eff}. This behavior, combined with the absence of the SiO_2 diffusion-barrier as a visual aid, presented a challenge to the determination of the junction position within the a-SiN_x:H-coated wires.

SPCM measurements performed at λ = 405 nm and λ = 650 nm both showed mild variations in E.Q.E. along the length of the a-SiN_x:H-coated wires (Fig. S9). However, the two measurements showed no common trends that might identify the start of the radial junction, suggesting that the variations were due to optical (rather than electrical) phenomena. In addition to the effects of the tapering wire-diameter described above (evident in λ = 650 nm SPCM images), the a-SiN_x:H-coated wires also exhibited optical artifacts due to the varying nitride thickness (evident at both SPCM

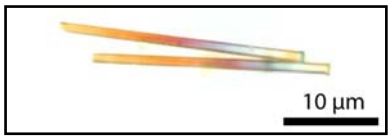

Figure S10. Optical micrograph of two a-SiN_x:H-coated Si microwires lying on a Ag substrate, showing coloration due to the variation in nitride thickness along the length of the wires.

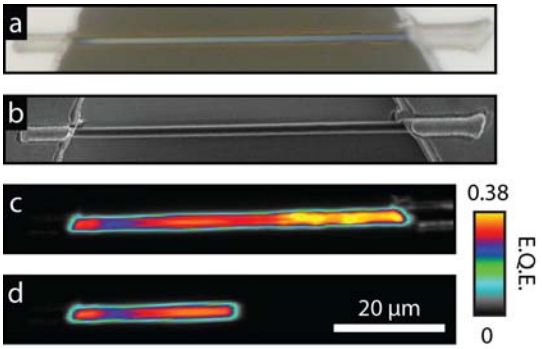

Figure S11. a, Optical microscope image, **b,** SEM image, and **c-d,** SPCM images of an a-SiN_x:H-coated single-wire device. The SPCM images were recorded before (c) and after (d) exposure to 30 keV electrons in the course of SEM imaging, and reveal the extent of the radial p-n junction.

wavelengths). As shown in Figure S3, the PECVD a-SiN_x:H films tapered from ~60 nm sidewall thickness at the wire base to ~120 nm sidewall thickness at the wire tip, which also led to apparent variations in the color of the wires under optical microscopy (Fig. S10).

To determine the location of the radial p-n junctions within the a-SiN_x:H-coated wires, it was found that irradiating them with 30 keV electrons in the course of scanning electron microscopy resulted in L_{eff} < 0.5 μm behavior within their axial regions. Thus, immediately following SEM imaging of the single-wire devices, the junction position could be observed by SPCM. Figure S11 shows the SPCM profiles for an a-SiN_x:H-coated device observed before (above) and after (below) SEM imaging, revealing an axial wire length of ~30 μm.

Calculation of τ_{eff} and S

Several previous studies have inferred effective bulk minority-carrier lifetimes (τ_{eff}) and surface recombination velocities (S) from minority-carrier collection length (L_{eff}) measurements in Si nano- and microwires.[1,4,16] The effective minority-carrier lifetime is related to the observed minority-carrier collection length by the standard relationship, $L_{eff} = \sqrt{D_n \tau_{eff}}$, where D_n is the minority-carrier (electron)

diffusion coefficient. For cylindrical structures such as Si wires, Allen et al. have provided equations relating τ_{eff} to the bulk minority-carrier lifetime, τ_n, the wire diameter, d_{Si}, and the surface recombination velocity, S, in the supplementary information of reference (16). For each SPCM measurement, we solved these equations numerically (ignoring bulk recombination), using the measured diameter of each wire (subtracting the estimated surface-coating thickness from the apparent diameter when appropriate), to obtain the value of S corresponding to surface-recombination-limited carrier transport. Because all Si microwires in this study were subject to identical high-temperature processing steps, we assumed that all the devices had identical bulk lifetimes (L_n >> 30 μm, τ_n >> 500 ns), and that variations in L_{eff} were due solely to different surface recombination velocities.

Spectral response of single-wire test structures

Spectral response measurements were performed on the champion single-wire test structures of each surface-coating type. The *J-V* characteristics of these devices appear in Fig. 4.

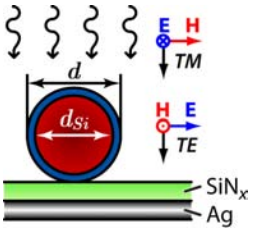

Figure S12. Schematic illustration of horizontal single-wire test structures and definition of the active device width, *d*. Substrates had > 100 nm evaporated Ag and ~300 nm PECVD SiN_x.

Figure S12 illustrates the cross-section of the single-wire devices in this configuration. Because the optical absorption of horizontally oriented microwires depends on the polarization of the incident light, and because the polarization state of our illumination source was not known, the spectral response of each device was measured twice, rotating the specimen 90° between measurements. The two measurements were then averaged to determine the spectral response of each wire to unpolarized light (such as sunlight). The photoresponse of each device was measured at short circuit (0 V) under uniform, collimated monochromatic illumination (λ = 300–1100 nm) using lock-in detection, and was normalized (by area) to that of a 3 mm diameter calibrated photodiode to determine the absolute external quantum efficiency (E.Q.E.) at each wavelength (Fig. S13a).

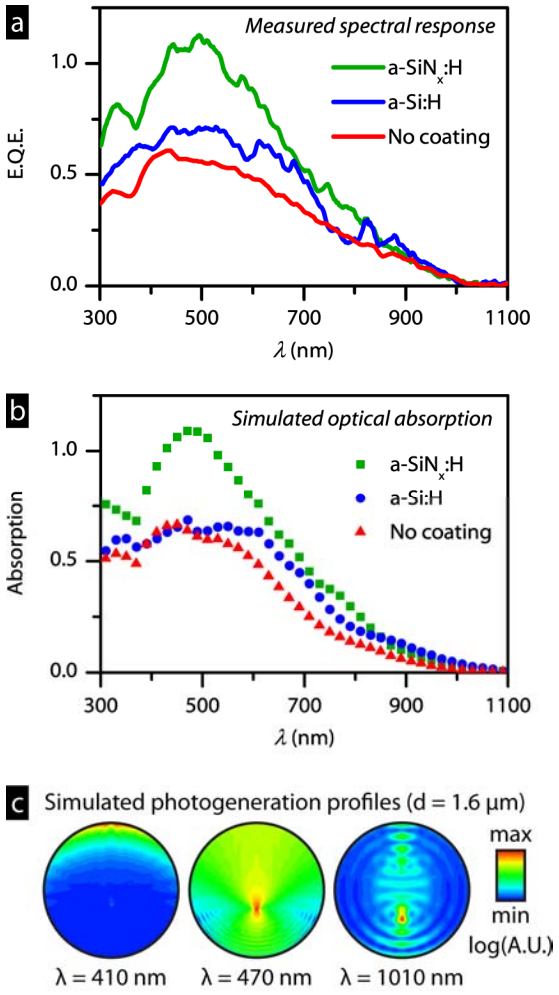

Figure S13. a, Measured spectral response of the champion single-wire device of each passivation type. External quantum efficiency (E.Q.E.) was determined based on the exposed physical area of each wire. **b,** Simulated optical absorption of each of the three devices plotted in (a). **c,** Simulated photogeneration profiles within the non-coated Si wire device at three selected wavelengths.

Following the convention of prior single-wire solar cell studies,[4,17-18] the exposed physical area of each wire* (observed by SEM; excluding that covered by the metal contacts) was used to calculate the E.Q.E. Interestingly, this normalization resulted in an apparent peak E.Q.E. of ~110% (near $\lambda = 500$ nm) for the a-SiN_x:H-coated single-wire device, warranting further investigation of the optical absorption and the effective area of these microstructures.

The observation of E.Q.E. > 100% can be explained by the photonic dimensions of the Si microwires (1.2–1.8 μm diameter). At this size regime, scattering theory predicts that particles can exhibit effective absorption cross-sections which exceed their physical cross-sections.[19] This enables Si microwires to interact with (and potentially absorb) more sunlight than predicted by physical area and conventional ray-optics.[5,15,20-21] Combined with the anti-reflectivity the a-SiN_x:H coatings, the relatively strong absorption of Si at $\lambda \sim 500$ nm, and the use of a back-reflecting substrate, this could lead to an apparent E.Q.E. exceeding >100% when the measured photocurrent is normalized to the optical power incident upon the physical area of the a-SiN_x:H-coated wire structure.

To further investigate the interaction of light with horizontal Si microwires, we simulated the optical absorption of each of the studied single-wire structures under the experimental configuration of Figure S12. Two-dimensional electromagnetic simulations were performed at 40 discrete wavelengths spanning the measurement range (λ = 310, 330, ... 1090 nm) using finite-difference time-domain software (FDTD Solutions, Lumerical). At each wavelength, the results of independent transverse-electric (TE) and transverse-magnetic (TM) simulations were averaged, and partial spectral averaging was applied to emulate unpolarized plane-wave illumination at normal incidence.† Each simulation took into account the measured wire diameter, the estimated surface-coating thickness, and the measured PECVD film optical properties (see Figs. S1 and S2), using tabulated optical constants[23] for Si and approximating the Ag substrate as an ideal metal boundary condition.

Figure S13c shows the simulated absorption profiles for the non-coated, d = 1.61 μm Si wire device at three selected wavelengths. At short wavelengths ($\lambda < 450$ nm), the absorption was concentrated near the wire surface, whereas at longer wavelengths ($\lambda > 500$ nm), the absorption was concentrated near the center of the wire. Following each simulation, the absolute absorption was calculated by dividing the total energy dissipated within the Si by the total energy of the plane wave incident above the cross-sectional width of the wire structure (d in Fig. S12). For comparison with experimental E.Q.E. measurements, the simulated absorption of the non-coated wire was reduced by 23% to account for the inactive (axial) portion of the champion cell (determined by SPCM.)

The simulated absorption of the horizontal wire structures (Fig. S13b) exhibited marked qualitative and quantitative agreement with the experimentally observed E.Q.E. of the single-wire solar cells. This suggests that the internal quantum efficiency (I.Q.E.) of the single-wire solar cells was close to 100% at all wavelengths, as previously predicted and measured for radial-junction Si microwires.[5,24] Both the measured E.Q.E. and simulated absorption of each device also predict similar J_{SC} values (weighted across the AM 1.5G spectrum) to those measured under calibrated solar illumination (Table S1), indicating good agreement between simulations and measurement techniques.

* For wires coated with SiO_2, a-Si:H, or a-SiN_x:H, the outer diameter of the wire structure (d) , rather than the diameter of the crystalline Si wire (d_{Si}), was used to calculate device area (see Fig. S12). For tapered wires, the average diameter was used.

† Partial spectral averaging[22] (PSA) suppressed resonance effects that were not experimentally observed due to mildly tapering wire diameter. The PSA width (Δf) was calculated based on simulation frequency (f) and Si refractive index (n_{Si}), as: $\Delta f = f / \left(1 + d_{Si} \cdot n_{Si} / \lambda\right)$.

Table S1. Measured outer diameter and assumed surface-coating film thickness (t_{film}) for the champion single-wire solar cells of each surface passivation type; and the short-circuit current density values measured under one-sun illumination, calculated based on E.Q.E. measurements, and calculated based on optical absorption simulations.

Surface coating	d (μm)	t_{film} (nm)	Short-circuit current density (mA·cm^{-2})		
			1-sun AM 1.5G (measured)	$\int_{AM1.5G}$ E.Q.E. (meas.)	$\int_{AM1.5G}$ Absorption (sim.)
None (SiO_2)	1.61	—	13.2	13.3	13.0
a-Si:H	1.45	8	16.2	16.9	15.7
a-SiN_x:H	1.47	70	22.5	22.7	21.1

The simulations also predicted a peak apparent absorption of 109% for the a-SiN_x:H-coated wire, confirming that the this structure's effective absorption area exceeds its physical cross-sectional area. This result does not violate conservation of energy, as the width of the plane wave excitation source was several times the width (d) of the wire. Thus E.Q.E. > 100% does not indicate non-conventional absorption processes (such as multiple exciton generation), nor does it reflect inaccurate measurement of physical area; rather, it illustrates the challenge in defining the active area of solar cells whose dimensions do not significantly exceed the illumination wavelength. Normalizing the performance of such solar cells to their physical area, although consistent with the conventions applied to macroscopic solar cells, can lead to apparent efficiencies which cannot be achieved over macroscopic areas. This property is beneficial for the use of single-wire solar cells as nanoelectronic power sources (as suggested by Tian, Kempa, et. al.).[17-18] However, when considering large-area (macroscopic) devices such as Si wire-array solar cells, the photovoltaic performance of each wire must be normalized to the effective per-wire absorption area (within the optical plane), regardless of the physical cross-sectional area of the wire. This motivates further experimental and theoretical studies to assess the true performance potential of macroscopic solar cells made from Si microwires, such as the efficiency projection for vertical wire-array solar cells presented in this paper. The potential efficiency of macroscopic solar cells made from arrays of *horizontally* aligned Si microwires has also been studied,[25] and is presented in the following section.

Efficiency potential for horizontal wire-array solar cells

Figure S14 illustrates a proposed horizontal-microwire-array solar cell structure in which the configuration of each individual wire closely resembles the experimental configuration of our single-wire test structures. The use of interdigitated back-side contacts provides a metallic back-reflector beneath each wire (analogous to the SiN_x-coated Ag substrates used for our single-wire devices), and would also eliminate any contact shading losses (which were ignored in our calculation of single-wire efficiency). Thus it seems reasonable to conclude that if such a structure could be fabricated, it could attain efficiencies on par with our single-wire solar

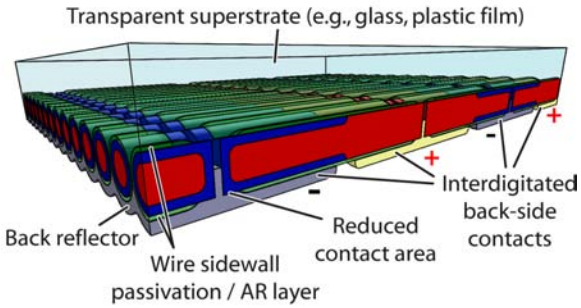

Figure S14. Proposed large-area wire-array solar cell consisting of aligned, tightly packed, horizontally oriented Si microwires with radial p-n junctions. Note that these authors have not attempted to fabricate such structures.

cells (i.e., up to 9%), assuming each wire had the electrical properties of our champion SiN_x-coated devices.

However, as discussed in the previous section, the photonic dimensions of Si microwires enable them to interact with (and potentially absorb) more light than predicted by their physical cross-sectional area (from a classical ray-optics perspective). Thus it is possible, for tightly packed arrays of horizontal microwires, that adjacent microwires could effectively "shade" one another without physically overlapping—which would result in lower large-area cell efficiencies than the apparent single-wire efficiencies. To investigate this effect, we have simulated and compared the optical absorption of Si microwires in an "isolated" configuration and an "arrayed" configuration, as depicted in Figure S15. The simulated wires had dimensions typical for our a-SiN_x-coated single-wire solar cells, and we employed the same modeling approach as was presented in our discussion of the spectral response of isolated single-wire solar cells (above). To extend our analysis to the arrayed configuration, we simply modified the simulation to apply periodic boundary conditions at either side of the wire.* The simulation results are plotted in Figure S15.

As expected, the presence of neighboring wires affected the simulated absorption of each wire. In particular, the phenomena of >100% apparent per-wire absorption did not occur for the arrayed wires, as this would have violated the conservation of energy. Indeed, the peak apparent absorption decreased from 112% for the isolated wire to 94% for the arrayed wire. However, the arrayed configuration was beneficial to absorption at other wavelengths (e.g., λ = 800 nm), which can be conceptualized

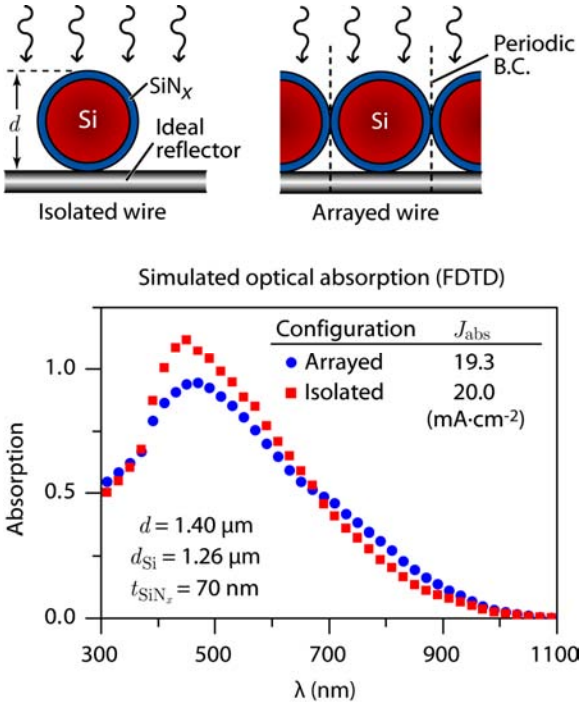

Figure S15. Simulated optical absorption of horizontally oriented Si microwires, in a tightly packed array configuration (depicted above right), and isolated as single-wire devices (left).

as light scattering between adjacent wires. Weighting the two simulated absorption spectra by the solar spectrum (AM 1.5G), we found that the photoabsorption current density (J_{abs}) differed by only 3.6% between the isolated horizontal wire (20.0 mA·cm^{-2}) and the arrayed horizontal wires (19.3 mA·cm^{-2}).

Thus, our single-wire measurements provide a reasonable indicator of the performance potential of solar cells made from densely packed, horizontally aligned Si microwires (i.e., their efficiency could approach ~8.7%), although the ill-defined areas of single-wire devices nonetheless prevent a true definition of their photovoltaic efficiency as individual devices.

There remain numerous unexplored and promising routes to significantly enhance the efficiencies of horizontal wire-array solar cells. Their performance could be improved, for example, by engineering the diameter and pitch of the wires so as to maximize dielectric

* "Isolated" wire simulations employed a *total-field scattered-field* (TFSF) source[22] (wider than the wire) with perfectly matched layer (PML) boundary conditions located several microns to either side of the wire. "Arrayed" wire simulations employed a plane-wave source with periodic boundary conditions immediately adjacent to either side of the wire.

resonance absorption enhancements, as proposed for nanowire solar cells.[15,20] Furthermore, the geometry seems particularly well-suited for the use of aligned, lenticular lens micro-optical concentrators like those demonstrated on Si microcells.[32] At present, however, the efficiencies of even our best single-microwire solar cells were greatly limited by incomplete optical absorption, as evidenced by their low J_{SC} and poor infrared spectral response despite our use of back-reflecting substrates and antireflective coatings. Thus we conclude that solar cells comprising arrays of horizontally oriented, crystalline Si microwires (such as that proposed in Figure S14) will require the use of larger-diameter wires than studied herein, or other breakthroughs in absorption engineering, in order to obtain photovoltaic efficiencies that rival wafer-based Si photovoltaics.

Effect of reflective substrates

In most prior reports of single-wire Si solar cells, Si_3N_4- and/or SiO_2-coated Si wafers were used as device substrates, as is common throughout the field of single-wire device research.[4,17-18,26-27] In this report, however, our single-wire solar cells were fabricated exclusively on SiN_x-coated Ag (on Si) substrates,* which improved their efficiency because Ag is a better back-reflector than Si. Figure S16 compares the measured reflectivity of a SiN_x-coated Ag substrate to that of a Si_3N_4-coated Si substrate.

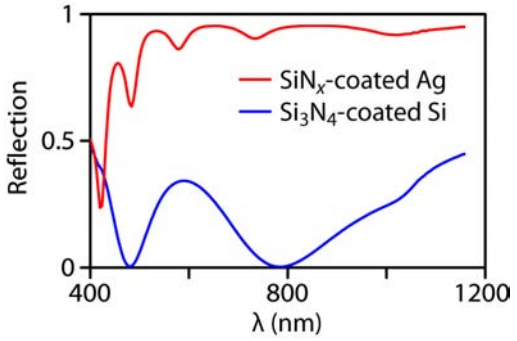

Figure S16. Measured reflectivity of a SiN_x/Ag/Si substrate that was used in this study vs. that of a Si_3N_4-coated Si wafer similar to those used as substrates in prior studies[4] (here, having 300 nm Si_3N_4). Data were measured at normal incidence.

An effective back-reflector is an integral component of virtually all thin-film solar cell designs. However, as pointed out in the review of this manuscript, the use of Ag substrates prevents comparison to prior single-wire solar cell literature. Thus, to investigate the degree by which the use of Ag substrates benefited the photovoltaic performance of these devices, as well as to allow better comparison to prior work, we performed the following simulations and measurements.

Using the FDTD simulation technique described above, we modeled the optical absorption of the three champion devices of each surface passivation type, shown in Figure S15. Each device was modeled on both a Ag and a Si substrate, assuming a 300 nm nitride layer thickness for either substrate type. We used the measured optical properties of our SiN_x films for the Ag substrate coating (Fig. S1) and tabulated optical properties of Si_3N_4 for the Si substrate coating.[28] Due to the high reflectivity of Ag across the solar spectrum (>96% for our evaporated films, see Fig. S6 of reference 5), the Ag layer was simply implemented as a metallic (i.e., 100%-reflecting) boundary condition in the FDTD simulations, whereas the Si substrate was modeled as an infinitely thick slab using tabulated optical properties of Si.[23]

Weighting the simulated optical absorption spectra of Figure S17 by the solar spectrum (AM 1.5G), we calculated the predicted J_{SC} of each device, for either substrate type, thus determining the *J_{SC} enhancement factor, F*, caused by the use of reflective Ag substrates. These values are shown in Table S2.

* A handful of devices of each type were also fabricated on sapphire substrates for SPCM measurements. These were not characterized as solar cells due to the difficulty of producing "fair" 1-sun illumination: light was reflected within the transparent wafers, effectively illuminating devices from below.

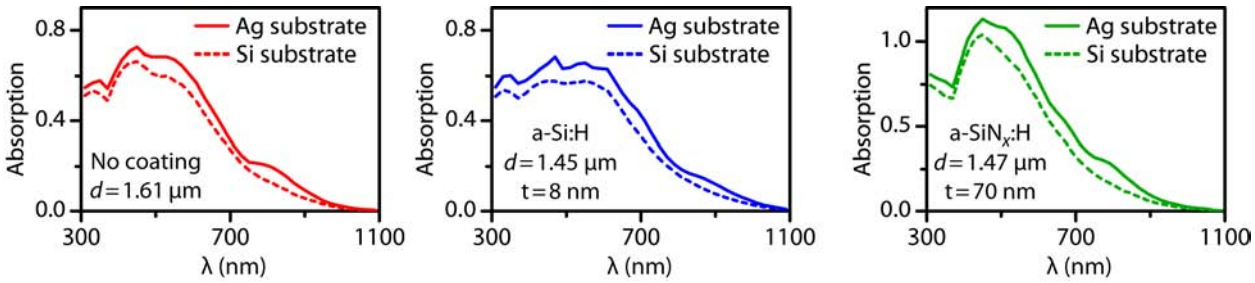

Figure S17. Simulated optical absorption spectra for the champion single-wire solar cells of each surface coating type on either Ag substrates with a 300 nm PECVD SiN_x insulation layer (solid lines) or Si substrates with a 300 nm Si_3N_4 insulation layer (dashed lines).

To estimate the efficiency that each champion cell would have obtained if fabricated on Si (rather than Ag) substrates, we measured their performance under reduced illumination levels (by defocusing the solar simulator) to produce J_{SC} values of $1/F$ times the originally measured one-sun J_{SC} values (while still normalizing photovoltaic efficiency to 100 mW·cm^{-2}). These results of these measurements are tabulated in Table S2 below. Due to the near-unity diode ideality factors of our devices, the 15%–18% attenuation of J_{SC} produced very little degradation of V_{OC} or FF.

These measurements suggest that using less-reflective Si substrates would have yielded 16%–20% lower photovoltaic efficiencies than were achieved in this study. Thus, highly reflective device substrates are an important and straightforward route to improving the efficiency of horizontally oriented single-wire or wire-array photovoltaic devices. However, we note that the key efficiency improvements presented in this work arose not from improvements in optical absorption or J_{SC} (as prior devices have obtained J_{SC} as high as 24 mA·cm^{-2});[17] but rather evince significant improvements in the V_{OC} and FF values achieved for VLS-grown crystalline Si microwire photovoltaics.

Table S2. Projected contribution of reflective substrates (SiN_x-coated Ag) to the photovoltaic performance of the champion single-wire solar cells of each passivation type (compared to Si_3N_4-coated Si substrates).

Champion device type	Simulated J_{SC} (mA·cm^{-2})		J_{SC} enhancement	Measured photovoltaic performance [a]					Relative η enhancement
	Ag subs.	Si subs.		Suns	J_{SC} (mA·cm^{-2})	V_{OC} (mV)	FF (%)	η [b] (%)	
Bare/SiO_2	13.0	11.0	**17.6%**	1.0	13.2	451	76.6	4.56	**19.2%**
				.850	11.2	446	76.2	3.82	
a-Si:H	15.7	13.3	**18.4%**	1.0	16.2	564	80.7	7.37	**19.5%**
				.844	13.7	561	80.3	6.17	
a-SiN_x:H	21.1	17.3	**21.6%**	1.0	22.5	535	75.0	9.04	**23.7%**
				.822	18.6	527	74.5	7.30	

[a] Measurements are reported with three significant figures of *relative* precision; however, note that our instrumentation provides only two significant figures of *absolute* precision for J_{SC} and η.

[b] Normalized to 100 mW·cm^{-2}, regardless of incident power density.

Optoelectronic simulation of Si wire-array solar cells

For this study we modified a previously-described electro-optical model of Si wire-array solar cells[4] to simulate a device of the specific wire dimensions, doping profiles, recombination rates, and thin-film optical properties reported herein; as well as to include light-trapping elements recently reported to enhance the optical absorption of Si wire arrays.[5,8] Details of the simulation methods and parameters beyond those presented here can be found in references 25 and 29. In comparison with the prior modeling, the most substantial changes were as follows:

- The wire length was increased (from 25 to 75 μm) while the diameter was decreased (from 3.0 to 1.6 μm)
- An 80 nm a-SiN_x:H anti-reflective / surface-passivation layer was added along the wire sidewalls, and Al_2O_3 light-scattering particles (400 spheres per unit cell) were randomly placed within the lower 50 μm of the PDMS infill material.
- Minority-carrier lifetime and surface recombination velocity were respectively increased and decreased to reflect the present observations of L_n = 30 μm and S = 70 cm·s^{-1} (vs. prior values of L_n ~ 10 μm and S ~ 10^3 cm·s^{-1}).

To simulate the performance of the large-area wire-array solar cell depicted in Figure 5a, a single unit cell was simulated using periodic boundary conditions. A 7 × 7 μm array pitch was chosen, corresponding to the Si wire arrays grown in this and other relevant studies.[5,8] Figure S18 depicts the simulated structure.

Full-field, three-dimensional electromagnetic simulations of the wire-array unit-cell were performed using commercial finite-difference time-domain simulation software (Lumerical Solutions). Table S3 specifies the optical properties of each material in the structure. To approximate normal-incidence sunlight, simulations were performed at each of seven discrete

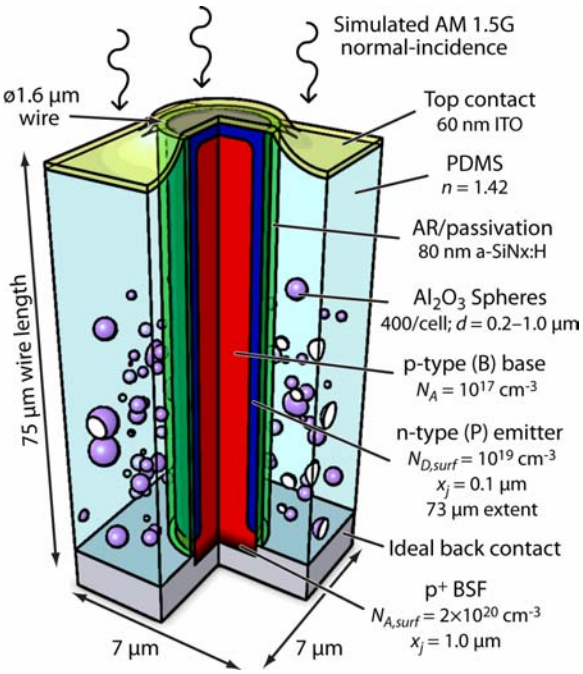

Figure S18. Schematic illustration of simulated wire-array unit cell, indicating the composition and dimensions of the structure, and the doping profiles within the Si wire.

Table S3. Optical properties used for simulations

Material	Optical properties
Si	Aspnes[23]
a-SiN_x:H	Fig. S1
PDMS	n = 1.4
ITO	Woollam[30]
Al_2O_3	Palik[28]
Back contact	Metallic boundary condition

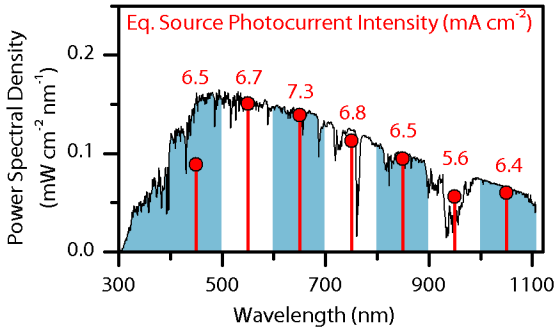

Figure S19. Simulation source intensities used to approximate AM 1.5G (100 mW·cm^{-2}) illumination.

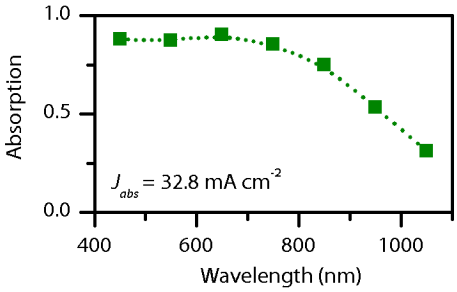

Figure S20. Optical absorption of the Si wire-array solar cell at each simulation wavelength.

wavelengths (λ = 450, 550, ... 1050 nm), with the results of each simulation weighted to yield the same equivalent source photocurrent (43.5 mA·cm^{-2}) and similar power spectral density as the λ = 280–1100 nm AM 1.5G spectrum, as shown in Figure S19. Following each simulation, the overall absorption and photogeneration profiles were calculated based on energy dissipation within the Si, then mapped to a two-dimensional cylindrical mesh for finite-element device physics simulations. Figure S20 plots the simulated optical absorption spectrum of the wire array, and Figure S21 plots the vertical cross section of the photogeneration profiles within the Si wire at each simulated wavelength.

Finite-element device physics simulations were performed using commercial electronic design automation software (Synopsys TCAD Sentaurus Device version A2009.06-SP1), to simulate the terminal current-voltage (*I-V*) behavior of the Si wire-array solar cell. The simulations were performed for the vertical Si wire device shown in Figure S18, using the photogeneration profiles calculated from optical simulations. The wire structure was simulated under cylindrical symmetry, using the drift-diffusion carrier transport model, and considering doping-dependent mobility and lifetime; Auger, SRH, and surface-SRH recombination; and Fermi carrier statistics.

The doping levels and junction profiles of the simulated structure were inferred from 4-point *I-V* measurements of single-wire devices as well as spreading resistance measurements of planar control wafers.[25] Unlike the single-wire solar

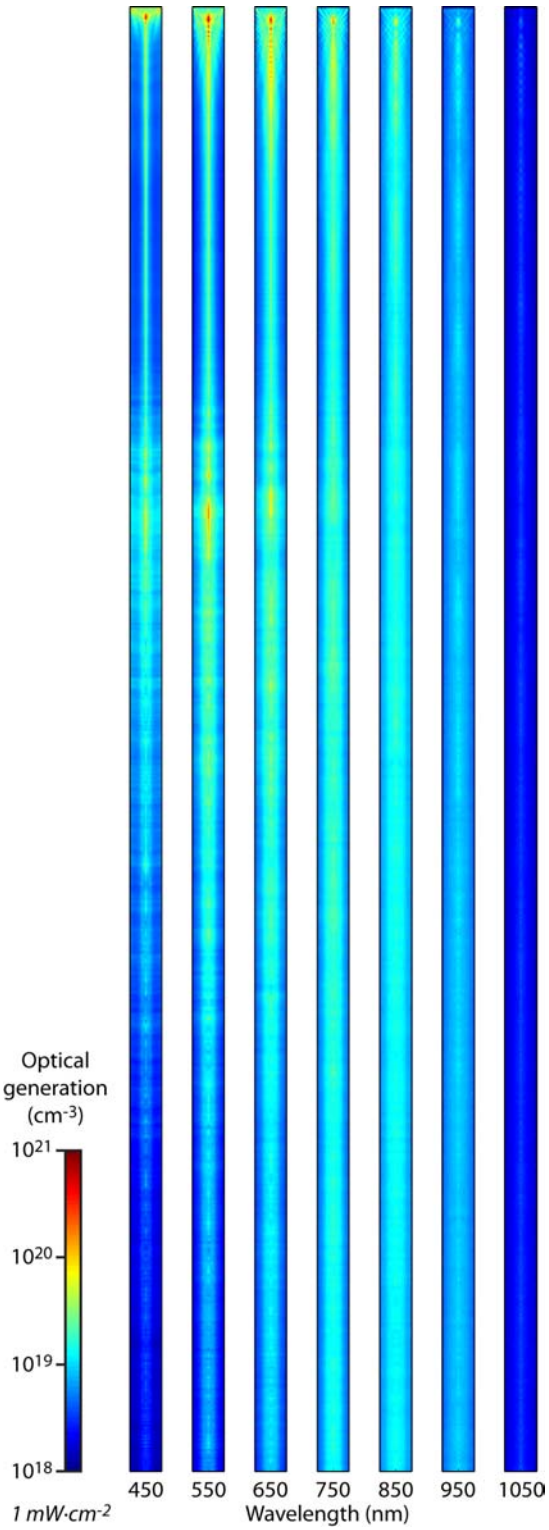

Figure S21. Simulated optical generation profiles within the wires of a Si wire-array solar cell under 1 mW·cm^{-2} illumination at each simulated wavelength. Wires are 75 μm in length, and the Al_2O_3 particle-infill occupies lower 50 μm of the array.

cells of this study, the simulated structures were assumed to have radial p-n junctions extending throughout all but the bottommost 2 μm of each wire. Recombination parameters were conservatively chosen based on the single-wire SPCM experiments: S = 70 cm·s^{-1} at the wire sidewalls and a limiting lifetime of τ = 500 ns throughout the wire. A standard SRV of 10^7 cm·s^{-1} was assumed for the (ohmic) top and bottom contacts. To explain the surprisingly low effective SRV of the Al:p-Si interface inferred by SPCM measurements, we hypothesize that the bottom contacts were effectively passivated by a p$^+$ back-surface field as shown in Fig. S18, which would be formed by thermal B diffusion from the p-type growth substrates (ρ < 0.001 Ω·cm) during the 2-hour thermal oxidation at 1100 °C.

The terminal *I-V* characteristics were simulated under each monochromatic illumination profile as well as the combined AM 1.5G illumination profile. The photocurrent was normalized to the 49 μm^2 area of the wire-array unit-cell to determine current density and photovoltaic efficiency (plotted in Fig. 5b and summarized in Table S4). Under monochromatic illumination, the simulated structure exhibited > 99% carrier collection efficiency at all wavelengths; thus, J_{SC} was limited solely by incomplete optical absorption of sunlight by the Si wires.

We note that these simulations predict slightly lower optical absorption (J_{abs} = 32.8 mA·cm^{-2}) than experimental studies have reported for similar Si wire-array geometries (J_{abs} = 35.9 mA·cm^{-2}). This was primarily due to the inclusion of an ITO top-contact in the simulated structure. In addition to the parasitic free-carrier absorption of this material at infrared wavelengths (λ > 950 nm), its relatively large refractive index (n = 1.4–2.0) also increased the front-surface reflectance loss of the structure at all wavelengths. Additional losses were caused by parasitic optical absorption within the a-SiN$_x$:H, particularly at blue wavelengths. These observations indicate that minimizing optical losses and parasitic absorption will remain a key requirement for the design of efficient Si wire-array solar cells.

Table S4. Simulation results

Simulated photovoltaic performance	
Open-circuit voltage	649 mV
Short-circuit current density	32.4 mA·cm^{-2}
Fill factor	83%
Efficiency	17.4%

References

1 Putnam, M. C. *et al.* 10 μm minority-carrier diffusion lengths in Si wires synthesized by Cu-catalyzed vapor-liquid-solid growth. *Applied Physics Letters* **95**, 163116 (2009).

2 Kayes, B. M. *et al.* Growth of vertically aligned Si wire arrays over large areas (>1 cm^2) with Au and Cu catalysts. *Applied Physics Letters* **91**, 103110 (2007).

3 Boettcher, S. W. *et al.* Energy-conversion properties of vapor-liquid-solid-grown silicon wire-array photocathodes. *Science* **327**, 185–187 (2010).

4 Kelzenberg, M. D. *et al.* Photovoltaic measurements in single-nanowire silicon solar cells. *Nano Letters* **8**, 710–714 (2008).

5 Kelzenberg, M. D. *et al.* Enhanced absorption and carrier collection in Si wire arrays for photovoltaic applications. *Nature Materials* **9**, 239–244 (2010).

6 Plass, K. E. *et al.* Flexible polymer-embedded Si wire arrays. *Advanced Materials* **21**, 325–328 (2009).

7 Takayama, S. *et al.* Topographical micropatterning of poly(dimethylsiloxane) using laminar flows of liquids in capillaries. *Advanced Materials* **13**, 570–574 (2001).

8 Putnam, M. C. *et al.* Si microwire-array solar cells. *Energy & Environmental Science* **3,** 1037–1041 (2010).

9 Forouhi, A. R. & Bloomer, I. Optical dispersion relations for amorphous semiconductors and amorphous dielectrics. *Physical Review B* **34**, 7018–7026 (1986).

10 Gu, Y. *et al.* Near-field scanning photocurrent microscopy of a nanowire photodetector. *Applied Physics Letters* **87**, 043111 (2005).

11 Gu, Y. *et al.* Local photocurrent mapping as a probe of contact effects and charge carrier transport in semiconductor nanowire devices. *Journal of Vacuum Science & Technology, B: Microelectronics Processing and Phenomena* **24**, 2172–2177 (2006).

12 Gu, Y., Romankiewicz, J. P., David, J. K., Lensch, J. L. & Lauhon, L. J. Quantitative measurement of the electron and hole mobility-lifetime products in semiconductor nanowires. *Nano Letters* **6**, 948–952 (2006).

13 Yeonghwan, A., Dunning, J. & Park, J. Scanning photocurrent imaging and electronic band studies in silicon nanowire field effect transistors. *Nano Letters* **5**, 1367–1370 (2005).

14 Yablonovitch, E., Allara, D. L., Chang, C. C., Gmitter, T. & Bright, T. B. Unusually low surface-recombination velocity on silicon and germanium surfaces. *Physical Review Letters* **57**, 249–252 (1986).

15 Cao, L. *et al.* Engineering light absorption in semiconductor nanowire devices. *Nature Materials* **8**, 643–647 (2009).

16 Allen, J. E. *et al.* High-resolution detection of Au catalyst atoms in Si nanowires. *Nature Nanotechnology* **3**, 168–173 (2008).

17 Tian, B. *et al.* Coaxial silicon nanowires as solar cells and nanoelectronic power sources. *Nature* **449**, 885–889 (2007).

18 Kempa, T. J. *et al.* Single and tandem axial p-i-n nanowire photovoltaic devices. *Nano Letters* **8**, 3456–3460 (2008).

19 Bohren, C. F. & Huffman, D. R. *Absorption and Scattering of Light by Small Particles*. (Wiley, 1983).

20 Cao, L. *et al.* Semiconductor nanowire optical antenna solar absorbers. *Nano Letters* **10**, 439–445 (2010).

21 Tsakalakos, L. *et al.* Interaction of light with Si nanowire films. *Conference Record of the Fourth IEEE World Conference on Photovoltaic Energy Conversion* 111–113.

22 FDTD Solutions User Guide v.6.5 (Lumerical Solutions, Inc., 2010).

23 Aspnes, D. E. in *Properties of Crystalline Silicon* (ed Robert Hull), 677 (INSPEC, IEE, 1999).

24 Kayes, B. M., Atwater, H. A. & Lewis, N. S. Comparison of the device physics principles of planar and radial p-n junction nanorod solar cells. *Journal of Applied Physics* **97**, 114302 (2005).

25 Kelzenberg, M. D. *Silicon microwire photovoltaics.* PhD thesis, California Institute of Technology (2010).

26 Dong, Y., Tian, B., Kempa, T. J. & Lieber, C. M. Coaxial group III nitride nanowire photovoltaics. *Nano Letters* **9**, 2183–2187 (2009).

27 Colombo, C., Heibeta, M., Gratzel, M. & Fontcuberta i Morral, A. Gallium arsenide p-i-n radial structures for photovoltaic applications. *Applied Physics Letters* **94**, 173108 (2009).

28 Palik, E. D. *Handbook of Optical Constants of Solids*. (Academic Press, 1997).

29 Kelzenberg, M. D., Putnam, M. C., Turner-Evans, D. B., Lewis, N. S. & Atwater, H. A. Predicted efficiency of Si wire array solar cells. *Proceedings of the Thirty-Fourth IEEE Photovoltaic Specialists Conference* (2009).

31 Woollam, J. A., McGahan, W. A. & Johs, B. Spectroscopic ellipsometry studies of indium tin oxide and other flat-panel display multilayer materials. *Thin Solid Films* **241**, 44–46 (1994).

32 Yoon, J. *et al.* Ultrathin silicon solar microcells for semitransparent, mechanically flexible and microconcentrator module designs. *Nature Materials* **7**, 907–915 (2008).